PAPER

First-principles based theoretical calculations of atomic structures of hydroxyapatite surfaces and their charge states in contact with aqueous solutions†

T. Saito, [ID] *a T. Yokoi, [ID] a A. Nakamura [ID] a and K. Matsunaga [ID] *ab

Surface charge states of biomaterials are often important for the adsorption of cells, proteins, and foreign ions on their surfaces, which should be clarified at the atomic and electronic levels. First-principles calculations were performed to reveal thermodynamically stable surface atomic structures and their charge states in hydroxyapatite (HAp). Effects of aqueous environments on the surface stability were considered using an implicit solvation model. It was found that in an air atmosphere, stoichiometric $\{0001\}$ and P-rich $\{10\bar{1}0\}$ surfaces are energetically favorable, whereas in an aqueous solution, a Ca-rich $\{10\bar{1}0\}$ surface is the most stable. This difference suggests that preferential surface structures strongly depend on chemical environments with and without aqueous solutions. Their surface potentials at zero charge were calculated to obtain the isoelectric points (pH_{PZC}). pH_{PZC} values for the $\{0001\}$ surface and the Ca-rich $\{10\bar{1}0\}$ surface were obtained to be 4.8 and 8.7, respectively. This indicates that in an aqueous solution at neutral pH, the $\{0001\}$ and Ca-rich $\{10\bar{1}0\}$ surfaces are negatively and positively charged, respectively. This trend agrees with experimental data from chromatography and zeta potential measurements. Our methodology based on first-principles calculations enables determining macroscopic charge states of HAp surfaces from atomic and electronic levels.

1. Introduction

Hydroxyapatite (HAp, $Ca_{10}(PO_4)_6(OH)_2$) is a main inorganic compound in human bones and enamels and is thus used in artificial bone grafts and implants. HAp also shows a high affinity for cells, proteins, and amino acids,[1–3] meeting a wide range of applications, including chromatography and drug delivery systems.[4,5] In such applications, HAp surfaces are considered to have positive or negative charge states depending on surface orientations and their relevant atomic structures and can attract various ions in body fluids and other aqueous solutions (*e.g.*, H^+, Ca^{2+}, OH^-, and PO_4^{3-}).[6] Surface charge states of HAp can also affect cell adsorption, crystal growth, and dissolution by electrostatically repelling and attracting ions or molecules with the surface charges.[7–10] It is thus essential to reveal the physical origin of the emergence of surface charges in HAp, with the goal of designing HAp-based biomaterials with excellent adsorption and bioactive properties.

HAp has a hexagonal structure with a space group of $P6_3/m$. Since HAp crystals typically have morphologies of hexagonal rods growing along the c axis or thin plates, two major surface planes are formed in large areas. One is the $\{0001\}$ surface (c plane), and the other is the $\{10\bar{1}0\}$ surface ($a(b)$ plane). According to previous experiments, positively charged lysozymes (LSZs) were more preferentially adsorbed on the $\{0001\}$ surface than the $\{10\bar{1}0\}$ surface, whereas negatively charged bovine serum albumins (BSAs) showed preference to be adsorbed on the $\{10\bar{1}0\}$ surface.[11–15] Therefore, it is believed that $\{10\bar{1}0\}$ and $\{0001\}$ surfaces are positively and negatively charged, respectively. It was also reported that surface zeta potentials of HAp crystal rods shifted from negative to positive values with increasing areas of the $\{10\bar{1}0\}$ surface.[16] In contrast, HAp crystals with a large area of the $\{0001\}$ surface was found to have more negative zeta potentials than those oriented isotropically.[17]

In earlier studies with chromatographic measurements, a physical origin of surface charge states in HAp was speculated in terms of possible atomic structures of $\{10\bar{1}0\}$ and $\{0001\}$ surfaces.[5,18–21] These studies indicated that HAp crystals have amphoteric adsorption properties of acidic (negatively charged) and basic (positively charged) proteins. Considering these results, Bernardi proposed that particular Ca and P sites at HAp surfaces can become absorption sites for acidic and basic

a Department of Materials Physics, Nagoya University, Nagoya 464-8603, Japan. E-mail: t-saito@nagoya-u.jp; kmatsunaga@nagoya-u.jp

b Nanostructures Research Laboratory, Japan Fine Ceramics Center, Nagoya 456-8587, Japan

† Electronic supplementary information (ESI) available. See DOI: 10.1039/d1ra06311a

proteins.[18] On the basis of the crystal structure of octacalcium phosphate $(Ca_8H_2(PO_4)_6 \cdot 5H_2O)$,[22] Kawasaki suggested that the $\{10\bar{1}0\}$ surfaces have vacant sites of OH^- ions and thus can serve as positively charged absorption sites, whereas the $\{0001\}$ surfaces have vacant sites of Ca^{2+} ions as negatively charged absorption sites.[5,20,21]

In the last decades, HAp surface structures have been experimentally investigated using scanning electron microscopy (SEM), transmission electron microscopy (TEM), and high-resolution transmission microscopy (HRTEM).[17,23,24] Sato et al. observed crystalline–amorphous interfaces of sintered HAp using HRTEM[25] and suggested that a nonstoichiometric $\{10\bar{1}0\}$ surface terminated at OH^- ions is one of the most stable surface structures. Ospina et al. applied a focal series reconstruction technique to HRTEM images and proposed that the $\{10\bar{1}0\}$ surface is terminated at a nonstoichiometric layer with flatly arranged Ca ions.[26] The presence of different surface terminations reported above is also supported by FTIR measurements combined with DFT calculations.[27–29] However, direct observations of atomic structures of HAp surfaces were not attained, probably because of difficulties of HAp-surface preparations and electron-beam damages.

In contrast, a number of theoretical calculations treated HAp surfaces in contact with water molecules and showed that two kinds of nonstoichiometric $\{10\bar{1}0\}$ surfaces are energetically favorable.[30,31] However, these studies considered the adsorption of a single H_2O molecule or a monolayer of H_2O molecules and did not explicitly account for the presence of an aqueous solution at the DFT level. It can thus be said that energetically favorable atomic structures of HAp surfaces in contact with aqueous solutions are still poorly understood. As a matter of course, the surface charge states and their physical origin have never been clarified.

In the current work, DFT calculations are performed to reveal thermodynamically favorable atomic structures of HAp surfaces and their charge states in contact with aqueous solutions. To model HAp surfaces in aqueous solutions, an implicit solvation model is employed in combination with DFT calculations. To obtain surface charge states of HAp in aqueous solutions, surface potentials at zero charge are calculated. Isoelectric points for HAp surfaces are finally estimated from their surface potentials to determine their surface charge states at the atomic and electronic levels.

2. Computational procedures

2.1 Electronic structure calculation

DFT calculations were performed with the projector augmented wave (PAW) method implemented in the Vienna Ab initio Simulation Package (VASP).[32] The generalized gradient approximation parameterized by Perdew, Burke, and Ernzerhof (GGA-PBE) was used to calculate the exchange-correlation potential.[33] Electrons of $3s^23p^64s^2$ for Ca, $3s^23p^3$ for P, $2s^22p^4$ for O and $1s^1$ for H were treated as valence electrons. Wave functions were expanded by plane waves with an energy cutoff of 800 eV, for which surface energies are found to sufficiently converge for both aqueous solution and vacuum. A $2 \times 2 \times 2$ k-point mesh

was used for a hexagonal unit cell of HAp. Atomic positions were optimized until atomic forces became less than 0.02 eV $Å^{-1}$. In these conditions, lattice parameters of the HAp unit cell were calculated to be 9.56 Å and 6.91 Å for the a and c axes, respectively. These values are in good agreement with experimental data, within an error of <1.3%.[34] Additionally, the diagonal components of stress tensor became small within 3×10^{-2} GPa and the others are negligible ($<10^{-7}$ GPa), suggesting that the current optimization successfully gets rid of internal stresses.

An implicit solvation model[35,36] based on the Poisson–Boltzmann equation was used to investigate a HAp surface immersed in an aqueous solution. If a solute/solvent system is treated only within DFT calculations, computational costs are very expensive due to a large number of solvent molecules. Alternatively, the implicit solvation model represents solvent molecules as a continuum dielectric, which corresponds to averaged molecular configurations of solvents. This approach greatly reduces computational costs by avoiding explicit consideration of solvent molecules. However, it is theoretically and experimentally suggested that strongly ordered water layers are present on apatite surfaces,[37–39] which are expected to decrease the dielectric constant of water near surfaces. Although the current implicit solvation model does not explicitly consider individual water molecules and thereby their ordering at surfaces, it represents the dielectric constant as a function of the electronic charge density of the solute/solvent, as described in the literature.[36] This formulation ensures a smooth decrease in the dielectric constant with decreasing distance from the surface. Implicit solvation was described with the default setting for water reported in the literature[35,36] (i.e., dielectric constant $\varepsilon_b = 78.4$, width of dielectric cavity $\sigma = 0.6$, cutoff charge density $n_{ck} = 0.0025$ $Å^{-3}$ and a surface tension parameter of 0.525 meV $Å^{-2}$). To describe an electronic double-layer region, a Debye length $\lambda_d = 3.0$ Å was used by assuming an aqueous solution containing 1 mol L^{-1} concentration of monovalent anions and cations at 298 K.

A number of different implicit solvation models are proposed and are used in different DFT-based programs. In order to assess the present methodologies, test calculations with the effective screening medium and the reference interaction site methods (ESM-RISM) implemented in QUANTUM ESPRESSO[40] were also performed. It was confirmed that the present results show the same trends in potentials of zero charge and isoelectric points for HAp surfaces. More details can be found in Section S1 in the ESI.†

2.2 Surface structures and slab models

To begin with, surface terminations of HAp are described. Here, $\{0001\}$, $\{10\bar{1}0\}$, and $\{11\bar{2}0\}$ surface planes of hexagonal HAp were considered since HAp crystal grains preferentially form hexagonal rods growing along the c axis. In order to prepare the surface slab models, it is advantageous to consider the stacking sequence of charge-neutral atomic layers. Fig. 1 illustrates atomic layers stacked in directions normal to the surface planes. The directions normal to $\{10\bar{1}0\}$ and $\{11\bar{2}0\}$ planes are
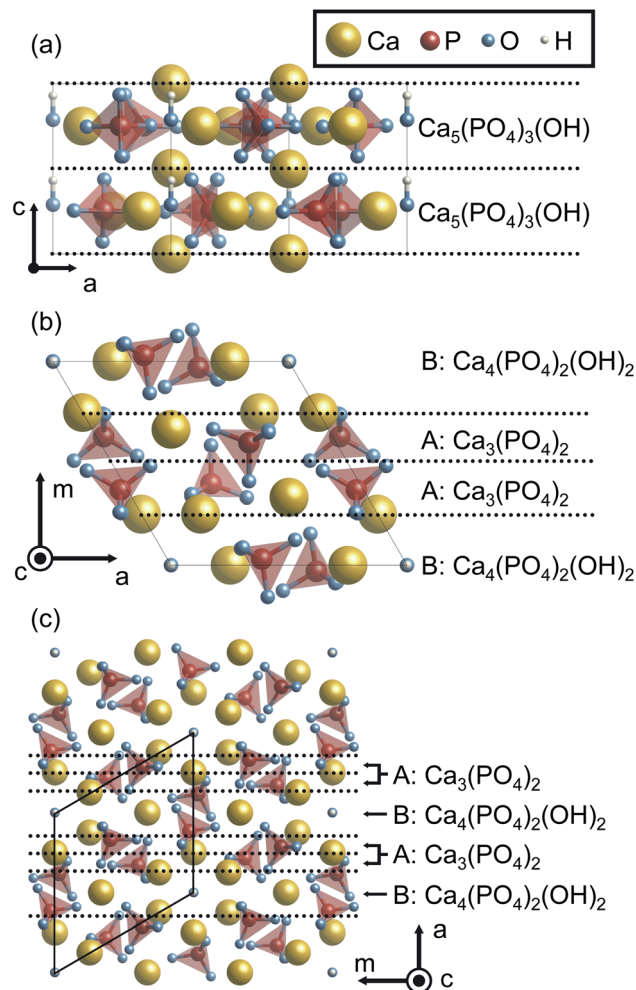
Fig. 1 HAp crystal structures viewed along the *m* and *c* axes. Stacking sequences of the atomic layers are indicated along the (a) *c*, (b) *m* and (c) *a* axes. The yellow, red, blue, and white balls represent Ca, P, O, and H atoms, respectively. In addition, PO₄ groups are represented by tetrahedra. Each layer is separated by the dashed lines. The composition of each layer is also indicated.

conventionally called the *m* and *a* axes for hexagonal crystals, respectively, and these notations are also used in the present study.

Along the *c* axis, the HAp crystal structure can be described by the stacking of stoichiometric atomic layers $Ca_5(PO_4)_3(OH)$. Therefore, the {0001} surface can always be stoichiometric. However, it should be noted that hexagonal HAp contains hydroxyl groups (OH^-) arranged along the *c* axis. Since it is assumed here that OH^- arrangements are not disordered but ordered along the *c* axis in the present study, two possible {0001} surface terminations of …–OH–OH (P-pole) and …–HO–HO (N-pole) can be generated.

Along the *m* and *a* axes, two different layers are alternately stacked (Fig. 1(b) and (c), respectively). One is the $Ca_3(PO_4)_2$ layer (A layer). This layer has a Ca/P molar ratio of 1.5, and thus is in the P-rich composition (the stoichiometric Ca/P molar ratio of 1.67). The other is the $Ca_4(PO_4)_2(OH)_2$ layer (B layer). This layer has a Ca/P molar ratio of 2.0, and can be called a Ca-rich

layer. It is noted that these off-stoichiometric Ca/P layers are charge neutral. As a result, HAp can be described by a stacking sequence of the two layers as …AABAAB… and thus three possible terminations for the surfaces were considered: …AAB (Ca-rich), …ABA (stoichiometric), and …BAA (P-rich).

When the surface slabs are generated, it is necessary to consider locations of Ca ions at the boundaries of the atomic layers to keep the surfaces charge-neutral and non-dipolar. Fig. 2 displays atomic configurations around the outermost atomic layers at the {0001}, {10$\bar{1}$0}, and {11$\bar{2}$0} surfaces. As can be seen in Fig. 2(a), the {0001} surface has two outermost Ca sites, denoted as Ca1 and Ca2. However, one of the Ca sites should be vacant due to the charge neutrality of the surface. Additionally, a {0001} surface formation leads to mirror symmetry breaking, and as a result, the Ca1 and Ca2 sites are crystallographically inequivalent. For these reasons, two different atomic configurations at the surface can be considered.

Similarly, the Ca- and P-rich {10$\bar{1}$0} surfaces contain three outermost Ca sites, one of which should be occupied and vacant, respectively (see Fig. 2(b) and (c)). Three different surface structures for each {10$\bar{1}$0} surface can be obtained, and two different surface structures are possible for the {11$\bar{2}$0} surface. In this study, these different atomic configurations for the surfaces were considered to determine the lowest-energy surface structures.

Based on the abovementioned considerations, the surface slab models were generated. The HAp unit cell was repeated by $1 \times 1 \times 2$, $1 \times 2 \times 1$, and $2 \times 2 \times 1$ for {0001}, {10$\bar{1}$0}, and {11$\bar{2}$0} surface slabs, respectively. Since two surfaces in each slab should be identical and it is desirable that these slabs for different surfaces have similar thicknesses, the stacking sequences of A and B layers were set to be A–A–B–A–A for the P-rich {10$\bar{1}$0}, B–A–A–B–A–A–B for the Ca-rich {10$\bar{1}$0}, and {11$\bar{2}$0} and A–A–B–A–A–B–A–A–B–A–A for the P-rich {11$\bar{2}$0} surfaces. Each slab was separated by a vacuum/solution layer with more than 14 Å thickness. It is noted that the two surfaces introduced in a {0001} slab are crystallographically different due to the directional arrangement of OH^- ions along the *c* axis, and thus N- and P-pole surfaces are formed. The OH^- arrangements may cause artificial electric fields through the surface slabs. In order to prevent this, the OH^- arrangements were modified to be symmetric with respect to the centers of the surface slabs, *i.e.*, HO–HO–OH–OH or OH–OH–HO–HO. With these OH^- configurations, the surface potentials of zero charge (described in Section 2.4) of the two surfaces were separately calculated. To calculate surface energies, the directional arrangement was adopted, as described in Section 2.3.

In order to check the dependences of surface energies and surface potentials on thicknesses of crystal and solution layers, test calculations in the implicit solvation model were performed. It was found that surface energies and surface potentials change by merely 2×10^{-3} J m^{-2} and 2×10^{-2} V, by increasing the solution layer from 14 Å to 29 Å. Similarly, it was also confirmed that the two quantities are little changed (5×10^{-3} J m^{-2} and 5×10^{-2} V) by increasing the crystal layer from 12 Å to 29 Å. Dilute concentrations of the solutes within 2 $\times$
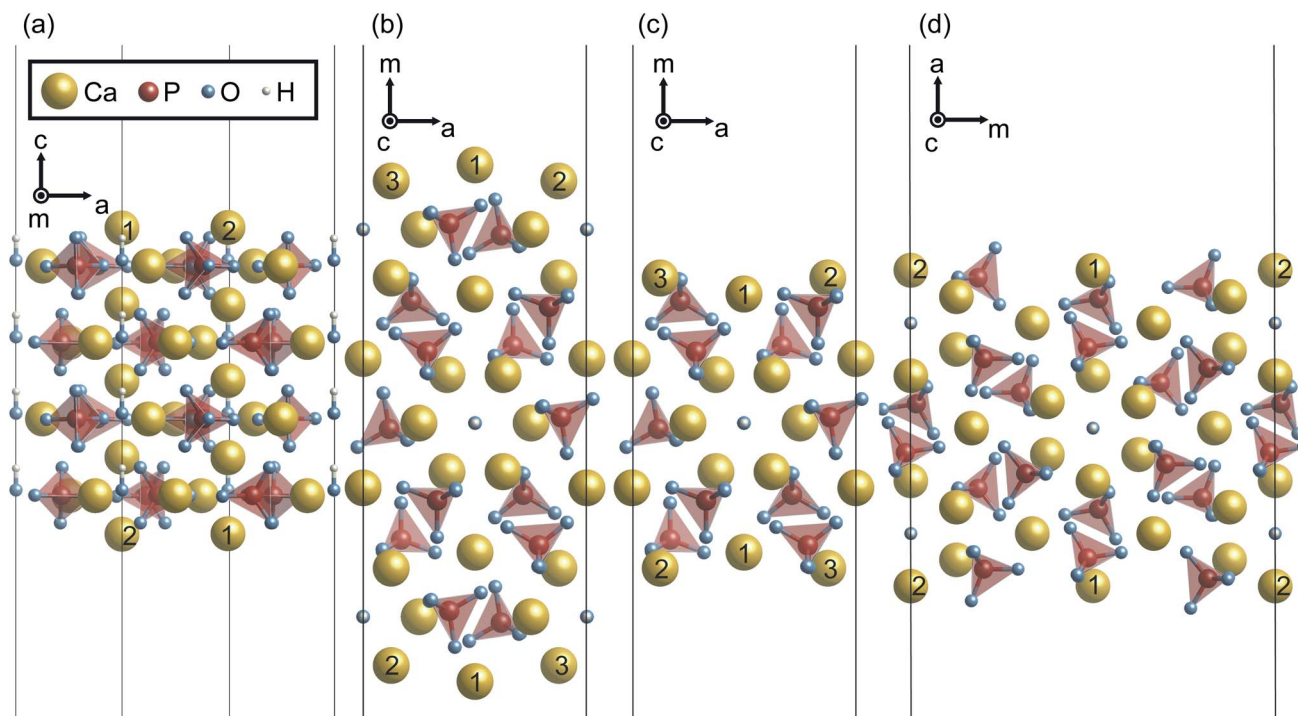
Fig. 2 Unrelaxed atomic structures of (a) stoichiometric {0001}, (b) Ca-rich {10$\bar{1}$0}, (c) P-rich {10$\bar{1}$0}, and (d) stoichiometric {11$\bar{2}$0} viewed parallel to the surface planes.

10^{-2} mol L^{-1} were also tested with $\lambda_d = 5.0$, 8.0, 10.0, and 20.0 for the Ca-rich {10$\bar{1}$0} surface. The surface energy and surface potential were found to be less sensitive to λ_d, with differences of 2×10^{-3} J m^{-2} and 3×10^{-2} V, respectively.

2.3 Surface energies and chemical potentials

Surface energy (ΔE_s) is defined as a difference in total energy between a bulk structure (E_t^{bulk}) and a surface slab (E_t^{slab}), as follows:

$$\Delta E_s = \frac{\left(E_t^{slab} - \frac{x}{2}E_t^{bulk} + \sum \Delta n_i \times \mu_i\right)}{2S},\tag{1}$$

where x is the number of Ca$_5$(PO$_4$)$_3$(OH) units in the surface slab, S is the surface area, μ_i is the chemical potential of the ionic species i, and Δn_i is the number of excess or lacking ions in the slab with respect to the stoichiometric composition. Depending on the chemical compositions of the surface slabs, the chemical potential term, $\sum \Delta n_i \times \mu_i$, is given by the following equations:

$$\sum \Delta n_i \times \mu_i = \begin{cases} 0, & \text{(stoichiometric)} \\ \mu_{Ca^{2+}} + \mu_{PO_4^{3-}} - \mu_{OH^-}, & \text{(Ca-rich)} \\ -\left(\mu_{Ca^{2+}} + \mu_{PO_4^{3-}} - \mu_{OH^-}\right). & \text{(P-rich)} \end{cases}\tag{2}$$

Two chemical equilibrium conditions were used to determine μ_i: a normal air atmosphere at a given temperature and an

aqueous solution at 298 K. In the air atmosphere, HAp was assumed to be in equilibrium with the CaO solid, O$_2$ gas, and H$_2$O gas at a particular temperature T. The partial pressures were set to $p_{O_2} = 0.21$ atm and $p_{H_2O} = 1 \times 10^{-5}$ atm. The chemical potentials of HAp and CaO were assumed to be equal to their total energies per unit formula obtained from DFT calculations. Chemical potentials for gaseous species are given by $\mu_g = \mu_g^\circ + k_b T \ln p_g$, where μ_g° is a standard chemical potential and k_b is the Boltzmann constant. μ_g° at 0 K was calculated from DFT calculations with an isolated molecule in cubic supercells of $15 \times 15 \times 15$ Å^3. The temperature dependence of μ_g° was taken from the thermodynamic data.[68]

It was assumed that the aqueous solution considered here is saturated with respect to HAp and that Ca^{2+}, PO$_4^{3-}$, HPO$_4^{2-}$, H$_2$PO$_4^-$, H$_3$PO$_4$, OH$^-$, and H$^+$ are dissolved in the aqueous solution. Their chemical potentials are given by

$$\mu_{i^{z+}} = \mu_{i^{z+}}^\circ + k_b T \ln a_{i^{z+}},\tag{3}$$

where $a_{i^{z+}}$ is the activity, and $\mu_{i^{z+}}^\circ$ is the standard chemical potential of an ionic species i^{z+} in the aqueous solution. The values of $\mu_{i^{z+}}^\circ$ were determined from DFT calculations and experimental thermodynamic data. As an example, for Ca^{2+}, $\mu_{Ca^{2+}}^\circ$ is provided by the reaction of Ca(s) + 2H$^+$(aq.) = Ca^{2+}(aq.) + H$_2$(g). The reaction provides the standard Gibbs energy of formation for Ca^{2+}(aq.) (ΔG_f°(Ca^{2+})). The value was obtained from the thermodynamic data.[69] Finally, $\mu_{Ca^{2+}}^\circ$ is obtained by

$$\mu_{Ca^{2+}}^\circ = \Delta G_f^\circ(Ca^{2+}) + \mu_{Ca}^\circ + 2\left(\mu_{H^+}^\circ - \frac{1}{2}\mu_{H_2}^\circ\right).\tag{4}$$

Notice that it is not necessary to evaluate the standard chemical potential of proton $(\mu^{\circ}_{H^+})$ because μ_{H^+} should be automatically canceled in eqn (2) due to the charge neutrality requirement.

In eqn (3), $a_{i^{z+}}$ is the product of the ionic concentration and the activity coefficient. Since HAp is hard to dissolve and thus its saturated solution can be considered as being dilute and ideal, the activity coefficients were assumed to be 1. Concentrations of ionic species were calculated from experimental data of the solubility product of HAp,[41] ionic products of water, and three phosphoric acids ($H_3PO_4 = H^+ + H_2PO_4^-$, $H_2PO_4^- = H^+ + HPO_4^{2-}$, $HPO_4^{2-} = H^+ + PO_4^{3-}$). The Ca/P molar ratio in the solution was considered to be the same as that of HAp. Ionic concentrations thus obtained as a function of pH are shown in Fig. S1 in the ESI.† Further details for the derivation of chemical potentials can also be seen elsewhere.[42–44]

2.4 Surface potentials of zero charge and isoelectric points

A potential of zero charge φ_{PZC} is generally defined as an electrostatic potential of a neutral electrode at which an electrode/electrolyte interface exhibits a net zero charge. This is experimentally determined with respect to a reference potential, and a conventional choice of the reference in electrochemistry is the standard hydrogen electrode (SHE). In contrast, an electrostatic potential of the bulk electrolyte is selected for reference in computational modeling with the implicit solvation model, which was also used in the present study.[35]

φ_{PZC} values for HAp surfaces with different orientations and atomic structures were evaluated using the surface slab models with the implicit solvation model. In principle, since a surface potential is defined as an electrostatic potential of a point charge at the surface with respect to that of a reference, φ_{PZC} for the surface slabs can be obtained from their Fermi energies E_f. When an electrostatic potential in the bulk electrolyte E_{ref} (the implicit aqueous solution in this study) is taken as a reference, φ_{PZC} can be obtained in the following manner.

$$\varphi_{PZC} = -\frac{E_f - E_{ref}}{eF}, \quad (5)$$

where e and F are the elementary charge and the Faraday constant, respectively. Here, E_{ref} was obtained from electrostatic potentials at the central points of the implicit solvents (furthest away from the HAp slab surfaces) in the supercells.

In general, it is considered that when oxide surfaces are immersed in aqueous solutions, hydration occurs, and the surfaces are terminated with hydroxyl groups in the neutral

state. The surface termination can be simply denoted as –MOH, where M means a cation on the surface. At a particular low pH condition, protons are enriched in the electrolyte, and the surface hydroxyl groups can interact with them to form –MOH$_2^+$. Then, the surface can take a positive charge. Inversely, at a larger pH condition, protons at the surface –MOH groups are dissociated and form H_2O with enriched OH^- groups in the aqueous solution so that the surface termination can be negative as –MO$^-$. Therefore, there is a pH of zero charge, which is called the isoelectric point pH_{PZC}.

As stated above, φ_{PZC} and pH_{PZC} indicates surface charge states in different ways. pH_{PZC} expresses a potential of zero charge φ_{PZC} in terms of pH. In this regard, McCafferty introduced the theoretical relationship between pH_{PZC} and φ_{PZC} on the basis of electrochemistry, and showed that φ_{PZC} is linearly proportional to pH_{PZC} for oxides as follows:[45]

$$\frac{\partial \varphi_{PZC}}{\partial pH_{PZC}} = -2 \times \frac{2.303RT}{F} = -0.120 \text{ V (at } T = 298 \text{ K)}, \quad (6)$$

where R is the gas constant. The above author also indicated that this relationship can be applicable irrespective of oxide substances. In this study, this linear function was obtained from surface potentials separately calculated for stoichiometric surfaces of several binary compounds along with their experimental isoelectric points. Table 1 lists the materials considered in this study, their surface planes, and experimental pH_{PZC} values.[46–51] For $CaCO_3$ (calcite), pH_{PZC} was measured using deionized water and preventing access of atmospheric CO_2 (ref. 52) because its pH_{PZC} is also affected by concentrations of Ca^{2+} and CO_3^{2-} groups in aqueous solutions.[53,54] φ_{PZC} values for the binary compounds were also calculated using surfaces with the lowest ΔE_s. Further details of the stable surfaces are described in Section S3 in the ESI.† As shown in Section 3.3, it was confirmed that even different materials firmly follow the same linear function with a gradient of −0.120 V.

3. Results and discussion

3.1 Surface energies in air atmosphere and aqueous solution

Fig. 3 shows the surface energies of HAp (ΔE_s) obtained under assumptions of the air atmosphere and the saturated aqueous solution. As stated in Section 2.2, the stoichiometric {0001} surface slabs have N- and P-pole surfaces. Because each of the {0001} surface slabs has both N- and P-pole surfaces, their averaged value of ΔE_s is represented in Fig. 3. In the air atmosphere (Fig. 3(a)), the stoichiometric {0001} surface has ΔE_s of

Table 1 Selected surface planes and experimental pH_{PZC} of binary compounds considered for evaluation of the relationship between φ_{PZC} and pH_{PZC} in this study (see Section 2.4). Averages of experimentally reported pH_{PZC} values are also written in the parentheses

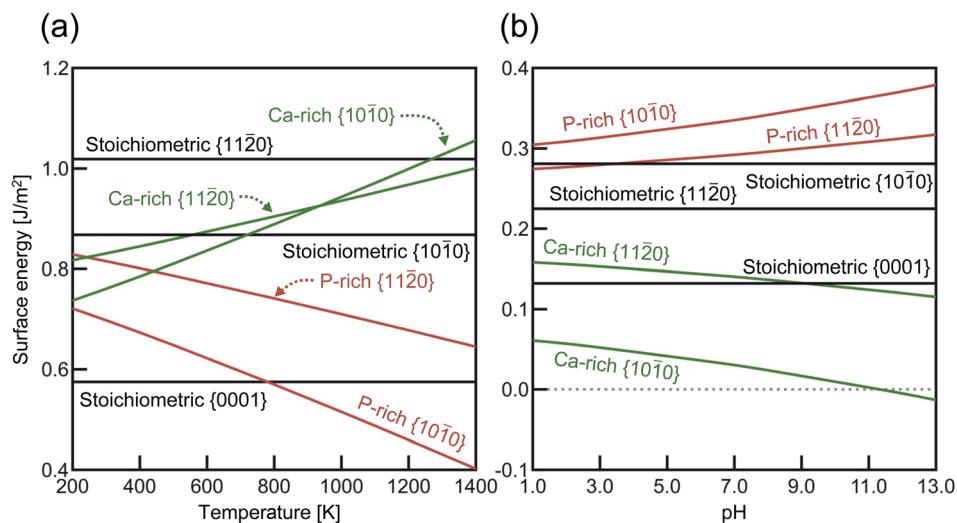| Material	Surface plane	Experimental pH_{PZC} (average)
MgO	{001}, {110}	12–12.5 (12.3)
SiO$_2$	{0001}, {10$\bar{1}$0}, {10$\bar{1}$1}, {$\bar{1}$011}	2.0–3.0 (2.5)
α-Al$_2$O$_3$	{0001}, {10$\bar{1}$0}, {11$\bar{2}$0}, {$\bar{1}$012}	8.2–9.2 (8.7)
CaCO$_3$	{10$\bar{1}$0}, {11$\bar{2}$0}, {10$\bar{1}$4}	5.4

Fig. 3 Calculated surface energies as a function of (a) temperature in the air atmosphere and (b) pH in the aqueous solution at 298 K. Black, green, and red lines correspond to stoichiometric, Ca-rich, and P-rich surfaces, respectively. For the respective terminations, surface structures showing the smallest total energies are selected, and their surface energies are plotted.

0.58 J m^{-2}, which is also the smallest of all below about 800 K. Among the lateral surfaces of $\{10\bar{1}0\}$ and $\{11\bar{2}0\}$, the P-rich $\{10\bar{1}0\}$ surface is most stable over the entire temperature range. This indicates that HAp crystal grains are surrounded by the stoichiometric $\{0001\}$ and the P-rich $\{10\bar{1}0\}$ surfaces when they are produced in the air atmosphere.

In the aqueous solution (Fig. 3(b)), the Ca-rich $\{10\bar{1}0\}$ surface has the lowest ΔE_s value in the entire pH range, even compared with the stoichiometric $\{0001\}$ surface. It is also interesting to see that the P-rich $\{10\bar{1}0\}$ surface has the highest ΔE_s value in aqueous solution, which is a quite in contrast to the case of the air atmosphere (see Fig. 3(a)). In the aqueous solution, the Ca-rich $\{10\bar{1}0\}$ surface is thus expected to be more preferentially formed than other P-rich $\{10\bar{1}0\}$ and $\{11\bar{2}0\}$ surfaces.

Previous DFT calculations indicated that the stoichiometric $\{0001\}$ surface has ΔE_s values of around 0.87 J m^{-2} under vacuum,[55,56] which are higher than our calculated value (0.58 J

m^{-2}) in Fig. 3(a). Considering that the other $\{0001\}$ surface had a similar ΔE_s value (0.86 J m^{-2}) under vacuum, this discrepancy probably comes from the difference in the Ca position at the outermost surface atomic layer. As stated in Fig. 2(a), there are two different $\{0001\}$ surface structures with respect to the outermost Ca sites, labeled as Ca(1) and Ca(2). It seems that the Ca(1) occupation corresponds to the one treated in the above-mentioned previous calculations, whereas, in the present study, the Ca(2) occupation is found to be energetically more stable with $\Delta E_s = 0.58 \text{ J m}^{-2}$. Such preference of the Ca(2) occupation is related to the coordination number of Ca(2). Fig. 4 displays atomic arrangements around the outermost Ca ions. At the $\{0001\}$ surface, Ca(1) has three first nearest neighboring (1st NN) O ions at distances of 2.19–2.26 Å. In contrast, Ca(2) has six 1st NN O ions at distances of 2.38–2.58 Å. The higher coordination number of Ca(2) to O ions would thus contribute to the smaller ΔE_s value.
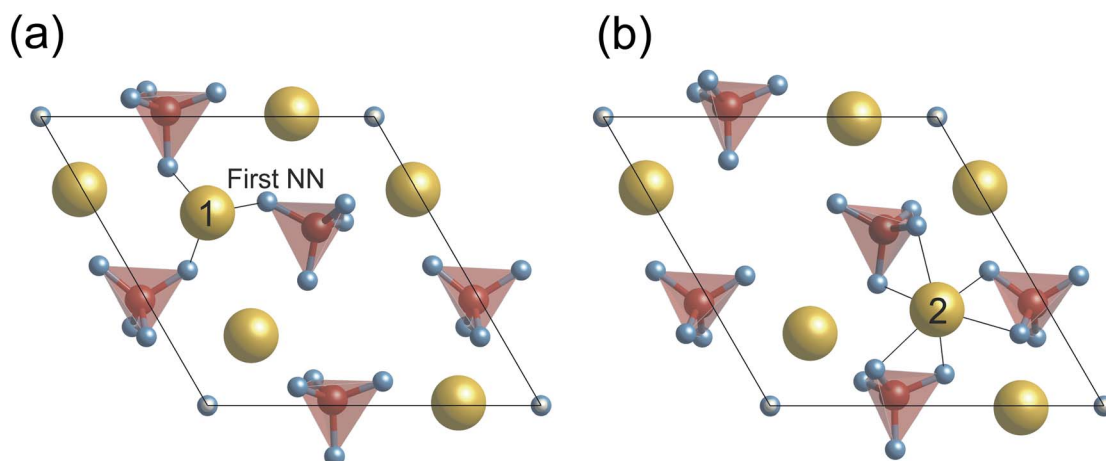

Fig. 4 Relaxed atomic configurations on the stoichiometric $\{0001\}$ surfaces with Ca^{2+} at (a) site 1 and (b) site 2, which are relaxed under vacuum. For clarity, only ions on top of the $\{0001\}$ surface are displayed.

Chiatti *et al.* performed similar DFT calculations and showed that in the air atmosphere, the stoichiometric $\{11\bar{2}0\}$ surface (1.22 J m^{-2}) is smaller in ΔE_s than for the stoichiometric $\{10\bar{1}0\}$ surface (1.35 J m^{-2}).[30] Their relative stability is different from the present results, *i.e.*, $\{10\bar{1}0\}$ (0.87 J m^{-2}) < $\{11\bar{2}0\}$ (1.02 J m^{-2}), as shown in Fig. 3(a). A plausible reason for this difference is the fact that the present stoichiometric $\{10\bar{1}0\}$ surface is more significantly relaxed than the previously reported one. The difference in the relaxed surfaces would arise from structural optimization methods. The present study uses a conjugate-gradient (CG) algorithm, while Chiatti *et al.* used a quasi-Newton algorithm. Regarding VASP, it is officially suggested that the implemented quasi-Newton algorithm fails badly when the initial structure is far from the local minimum energy.[70] In order to check the effect of the optimization methods, the two stoichiometric surfaces were thus again optimized using another quasi-Newton algorithm based on RMM-DIIS.[57] As a result, the ΔE_s value of $\{10\bar{1}0\}$ (1.09 J m^{-2}) is found to be larger than that of the $\{11\bar{2}0\}$ surface (1.02 J m^{-2}). The $\{10\bar{1}0\}$ surface obtained by the quasi-Newton algorithm is also less relaxed than that obtained by the CG algorithm. This suggests that the choice of an appropriate optimization algorithm is very important to find reasonable relaxed surfaces in structural relaxation calculation. However, the surface energies obtained by the quasi-Newton algorithm still are larger than those displayed in Fig. 3(a). It can be thus said that the relaxed surface structures obtained by the CG method should be more appropriate to represent the stoichiometric surfaces. More details are provided in Section S4 in the ESI.†

The surface energies for different surface orientations may be reflected in real HAp crystal shapes. For instance, HAp samples prepared by solution-precipitation methods typically have rod- or needle-like morphologies.[16,58,59] Since the HAp crystal structure is hexagonal, such morphologies indicate that the lateral $\{10\bar{1}0\}$ surface is much more stable than the $\{0001\}$ one, as can be seen in Fig. 3(b). Moreover, Liu *et al.* showed that HAp whiskers prepared by a hydrothermal method increase their aspect ratios with increasing pH from 6 to 9.[60] This trend could also be expected from the increasing difference in ΔE_s between $\{10\bar{1}0\}$ and $\{0001\}$ with rising pH values (see Fig. 3(b)). On the other hand, Wang *et al.* investigated shape changes of HAp nanosized crystal rods at high temperatures, and showed that HAp nanorods gradually increase their $\{0001\}$ surface areas in the temperature range of 300–700 °C.[61] This indicates less stability of the P-rich $\{10\bar{1}0\}$ surface than the $\{0001\}$ surface below 800 K (see Fig. 3(a)) in the air atmosphere, whose trend is also in good agreement with Fig. 3(a).

Regarding the nonstoichiometric $\{10\bar{1}0\}$ surface, the present calculations showed that the different chemical environments offer different atomic terminations: the P-rich one in the air atmosphere and the Ca-rich one in the aqueous solution (see Fig. 3). Although transmission electron microscopy should be a powerful means to identify such atomic structures, it is quite difficult to do so because HAp crystals seem to be easily subjected to electron-beam damages.[25] In this regard, Sato *et al.* performed HRTEM observations of HAp crystals sintered at a high temperature and observed the facetted $\{10\bar{1}0\}$ surfaces in contact with amorphous HAp due to electron-beam damages. These authors determined that the facetted $\{10\bar{1}0\}$ surfaces are the Ca-rich surfaces.[25] However, since the observed $\{10\bar{1}0\}$ surface is not a free surface that is treated in the present calculations, comparisons with the present results are not straightforward.

3.2 Surface atomic structures with and without an aqueous solution

In this section, characteristic atomic structures of surfaces in the different surrounding environments are investigated. Fig. 5
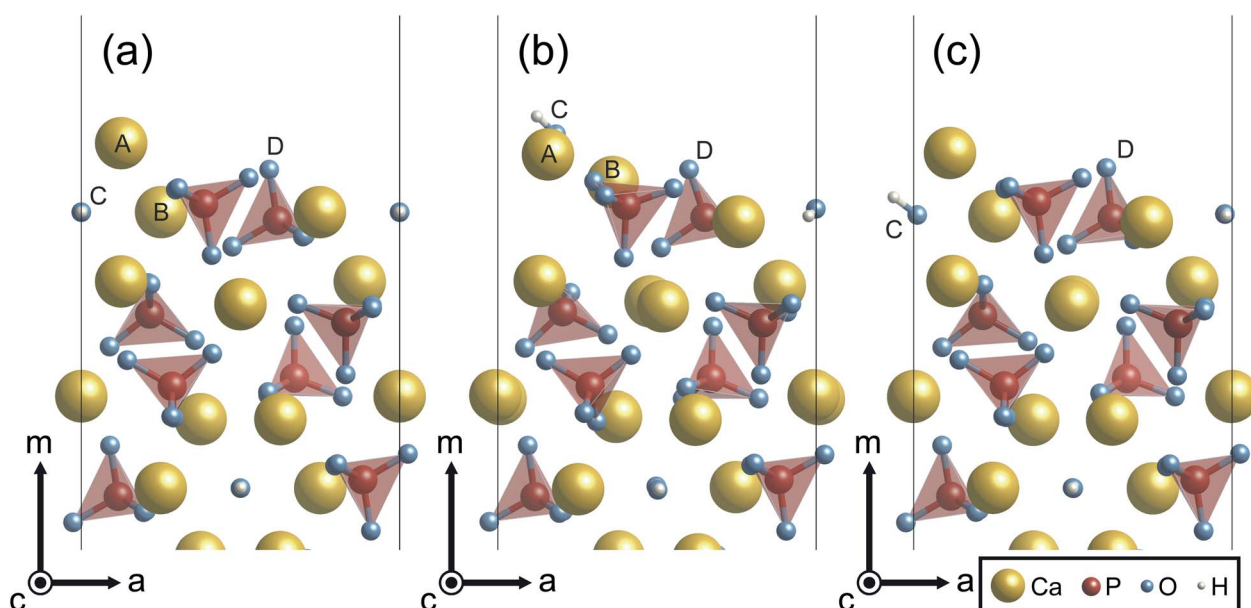

Fig. 5 Atomic configurations of the Ca-rich $\{10\bar{1}0\}$ surface viewed along the *c* axis. (a) The unrelaxed structure, (b) the relaxed structure under vacuum, and (c) the relaxed structure with implicit solvation.
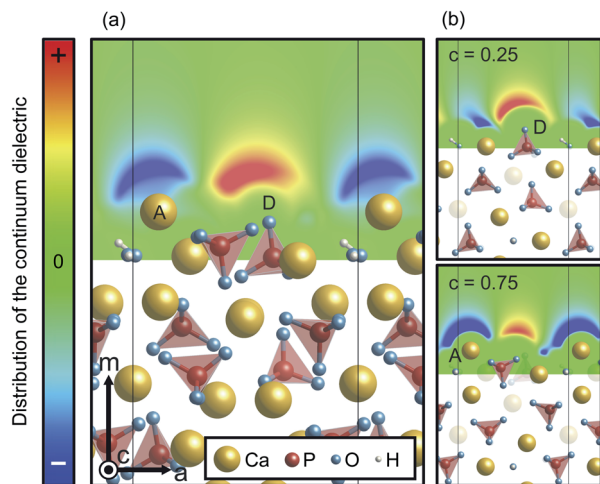
Fig. 6 Distribution of the continuum dielectric, which indicates the ionic charge density of the electrolyte, (a) averaged along the c axis and (b) around O(D) and Ca(A) ions on the Ca-rich $\{10\bar{1}0\}$ surface. For the color scheme, its maximum (colored red) and minimum (blue) values were set to 1×10^{-10} and -1×10^{-10} e$^-$ Å^{-3}, respectively.

shows the unrelaxed and relaxed atomic structures at Ca-rich $\{10\bar{1}0\}$ surfaces. For the unrelaxed surface (Fig. 5(a)), the surface has a protruding Ca ion at its outermost site (labeled A). As shown in Fig. 5(b), the relaxed surface under vacuum involves significant surface relaxations: the Ca(A) ion is displaced by 0.83 Å from its original position toward the crystal, while the Ca(B) and an OH(C) ions are also displaced by 1.40 Å and 3.06 Å away from the surface, respectively. Such large atomic relaxations take place so as to make more Ca–O bonds around the surface plane.

In contrast, however, the surface in contact with the implicit solvent (Fig. 5(c)) exhibits much smaller atomic displacements. This is because missing Ca–O bonds at the surface can be compensated by electrostatic interactions of surface ions with charges formed on the surface of the solvent, as is clearly seen in Fig. 6. The negative and positive charges are induced in the solvent surface across the outermost Ca(A) and O(D) ions. Such smaller atomic relaxations and electrostatic interactions with

the aqueous solution should lead to stabilization of the Ca-rich $\{10\bar{1}0\}$ surface shown in Fig. 3(b).

Unlike the Ca-rich $\{10\bar{1}0\}$ surface, the $\{0001\}$ and the P-rich $\{10\bar{1}0\}$ surfaces, which are stable in the air atmosphere, show minor relaxations both under vacuum and in the implicit solvent, as displayed in Fig. 7. It is noted that only the P-pole $\{0001\}$ surface is displayed in Fig. 7 because the relaxed P- and N-pole $\{0001\}$ surface structures are found to be quite similar. For the two surfaces, the surface ions are displaced by only ~0.8 Å under vacuum and ~0.6 Å in the implicit solvent. Such smaller atomic relaxations of the $\{0001\}$ and the P-rich $\{10\bar{1}0\}$ surfaces arise from their original atomic arrangements. For example, the outermost Ca(A) ion in the Ca-rich $\{10\bar{1}0\}$ surface (see Fig. 5) looks protruding from the underlying PO_4^{3-} and OH$^-$ ions. This results in its small coordination numbers with the 1st NN and 2nd NN ions. As compared with Ca(A) of the Ca-rich $\{10\bar{1}0\}$ surface, outermost Ca ions of the $\{0001\}$ and the P-rich $\{10\bar{1}0\}$ surfaces are located closer to the inner crystal layers, indicating their larger coordination numbers within 2nd NN ions. Owing to such more closely packed surface atomic arrangements, the $\{0001\}$ and the P-rich $\{10\bar{1}0\}$ surfaces display smaller surface relaxations, irrespective of the surrounding surface environments.

3.3 Potential of zero charge and isoelectric point

Based on the relaxed surface structures in the implicit solvent, their φ_{PZC} values are evaluated using eqn (6), as summarized in Table 2. The stoichiometric P-pole and N-pole $\{0001\}$ surfaces have almost the same φ_{PZC} values, and the $\{10\bar{1}0\}$ surfaces tend to exhibit smaller φ_{PZC} values. Among the $\{10\bar{1}0\}$ surfaces, the Ca-rich one, which is energetically most stable in the aqueous solution (Fig. 3), has the smallest φ_{PZC} value of 3.7 V. In order to reduce the surface potentials, surfaces with larger φ_{PZC} values in the aqueous solution can attract more negative hydroxyl ions. This can be rephrased by stating that the $\{0001\}$ and ($\{10\bar{1}0\}$) surfaces with larger (smaller) φ_{PZC} tend to take more negative (positive) charges.

The above results fairly agree with conventional views of surface charge states of HAp crystals: the $\{0001\}$ plane of HAp is negatively charged while the $\{10\bar{1}0\}$ plane is positively
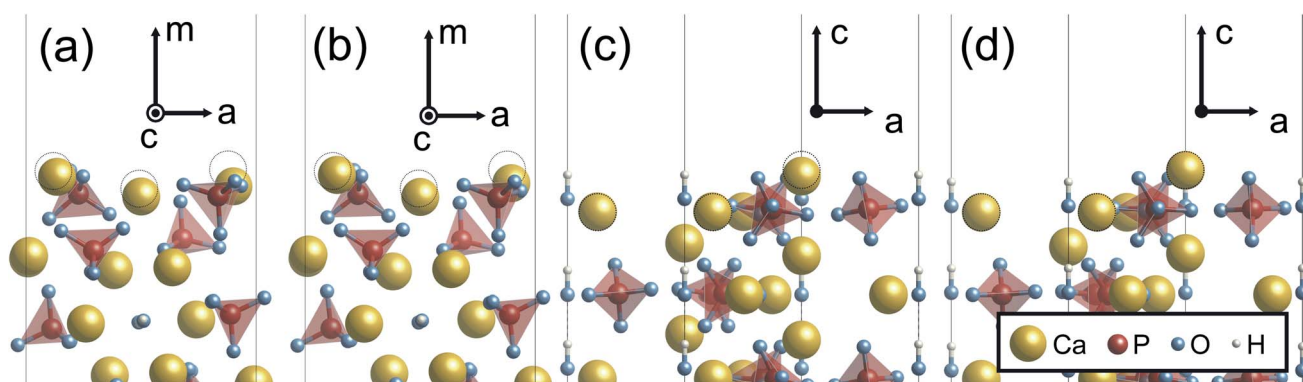

Fig. 7 Relaxed atomic structures of P-rich $\{10\bar{1}0\}$ and P-pole $\{0001\}$ surfaces. (a) Relaxed P-rich $\{10\bar{1}0\}$ under vacuum, (b) relaxed P-rich $\{10\bar{1}0\}$ in the implicit solvation, (c) relaxed P-pole $\{0001\}$ under vacuum, (d) relaxed P-pole $\{0001\}$ in the implicit solvation. Broken circles indicate original Ca positions before relaxation.

Table 2 Potentials of zero charge φ_{PZC} for the $\{0001\}$ and $\{10\bar{1}0\}$ surfaces with different terminations

Surface		Surface potential φ_{PZC} [V]
$\{0001\}$	P-pole	4.1
	N-pole	4.2
$\{10\bar{1}0\}$	P-rich	3.9
	Ca-rich	3.7
	Stoichiometric	4.0

charged.[11,16,17] This was understood from a conventional idea from chromatographic measurements that the $\{0001\}$ surface is rich in PO_4^{3-} ions and the $\{10\bar{1}0\}$ surface is rich in Ca ions.[5,18–21] The present results can support this idea because the Ca-rich $\{10\bar{1}0\}$ surface and the stoichiometric $\{0001\}$ surface (relatively PO_4-rich) are most stable when HAp is in contact with an aqueous solution. The anisotropy of the surface charge states of HAp $\{0001\}$ and $\{10\bar{1}0\}$ can lead to various pH_{PZC} values depending on morphologies of HAp crystal grains, which were experimentally reported.[6,17,62,63] Aizawa et al. also showed that surface zeta potentials of HAp shift from negative to positive values with increasing $\{10\bar{1}0\}$ surface areas at pH = 7.[16] The present results can reasonably explain these experimental data on the basis of atomic-level structures of HAp $\{0001\}$ and $\{10\bar{1}0\}$ surfaces.

As stated in Section 2.4, surface charge states of crystal grains are usually discussed by experimentally measurable pH_{PZC} in electrochemistry and biochemistry. Therefore, pH_{PZC} values of the energetically most stable Ca-rich $\{10\bar{1}0\}$ and $\{0001\}$ surfaces in HAp are evaluated according to eqn (6) in Fig. 8. As proposed by McCafferty,[42] it can be confirmed that φ_{PZC} has a linear relationship with pH_{PZC} irrespective of oxide substances. On the basis of this relationship, the pH_{PZC} values

are estimated to be 4.0, 4.8, and 8.7 for the N-pole $\{0001\}$, P-pole $\{0001\}$, and Ca-rich $\{10\bar{1}0\}$ surfaces, respectively.

The pH_{PZC} indicates a pH value where protons and hydroxyl ions are balanced so that a surface is charge neutral. When a particular pH value is considered and is larger than pH_{PZC}, the surface should be enriched with hydroxyl ions, resulting in a negatively charged surface. This is applicable to the stoichiometric $\{0001\}$ surface because the physiological pH is 7.4, and the pH range from 5.0 to 9.0 is often used in the processing of HAp crystal grains. Conversely, the Ca-rich $\{10\bar{1}0\}$ surface having the larger pH_{PZC} value tends to be positive. It can be said, therefore, that the present analyses can provide a quantitative description of the surface charge states of HAp crystal grains when they are immersed in aqueous solutions.

In the present study, DFT based theoretical analyses on surface charge states of HAp were carried out. It was found that the present methodologies can provide reasonable and quantitative descriptions of surface charge states, which should be promising to attain a theoretical understanding of atomic-level interactions with molecules and proteins in oxides and inorganic compounds as well as in calcium phosphates. It should be noted, however, that real surfaces may contain point defects and impurities, which may also affect the surface charge states. In fact, Yin et al. showed that zeta potentials of HAp are changed by not only pH values but also concentrations of Ca^{2+} and phosphate groups in the surrounding aqueous solution.[6] Carbonate group and Na^+ in aqueous solutions may also be included on the real surfaces.[63,64] It can be expected that these issues can be theoretically clarified on the basis of the present methodologies, which should be addressed in future works.

It also should be noted that all water molecules were implicitly treated in the current study. For future studies considering explicit water molecules, the results will be validated using the revised Tao-Mo (revTM) functional, which is known to provide accurate water properties.[65–67] It was found that the revTM provides more accurate lattice parameters of the HAp unit cell of 9.44 Å and 6.91 Å for the a and c axis, respectively, than the PBE functional with respect to the experimental data.[34] On the other hand, the revTM predicts slightly higher surface energies than the PBE, to be 0.23 J m^{-2}, 0.41 J m^{-2}, and 0.39 J m^{-2} for the stoichiometric $\{0001\}$, $\{10\bar{1}0\}$, and $\{11\bar{2}0\}$ surfaces, respectively. However, the order of the surface stability, namely $\{0001\} > \{11\bar{2}0\} > \{10\bar{1}0\}$, is the same as the PBE. The Ca-rich $\{10\bar{1}0\}$ surface has the φ_{PZC} value lower by 0.8 V than the P-pole $\{0001\}$ surface. The result suggests a low pH_{PZC} value of the Ca-rich $\{10\bar{1}0\}$ surface over the P-pole $\{0001\}$ surface, which is also consistent with that provided by the PBE. Accordingly, the revTM functional would provide similar results as PBE, and be applicable to the investigation of HAp surfaces with explicit solvent.

4. Conclusions

HAp surface structures and their charge states were examined using first-principles based calculations. An implicit solvation model was employed to model HAp surfaces immersed in aqueous solutions. The present calculations demonstrated that
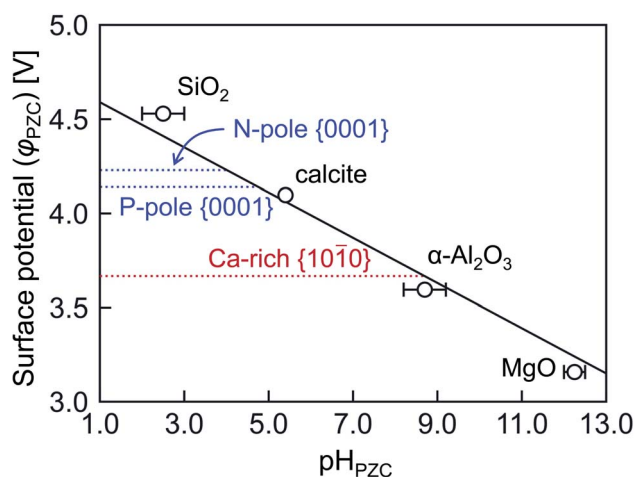
Fig. 8 Surface potentials φ_{PZC} plotted against pH_{PZC}. The solid line with a gradient -0.120 V was obtained by least square regression according to the theoretical linear function proposed in ref. 45.

© 2021 The Author(s). Published by the Royal Society of Chemistry

the stoichiometric {0001} and the P-rich {10$\bar{1}$0} surface are energetically most favorable, depending on the temperature, whereas in an aqueous solution, the Ca-rich {10$\bar{1}$0} surface becomes most stable. This suggests that the presence of an aqueous solution is critical in determining the preference of surface terminations. On the basis of optimized surfaces, their surface potentials at zero charge were calculated to obtain the isoelectric point (pH$_{PZC}$) of each surface. pH$_{PZC}$ values were found to be 4.8 and 8.7 for the {0001} surface and the Ca-rich {10$\bar{1}$0} surface, respectively. It can be said that the {0001} and Ca-rich {10$\bar{1}$0} surfaces are thus negatively and positively charged, respectively, in the aqueous solution at neutral pH. The anisotropy of surface charge states agrees with previous suggestions based on chromatographic behavior and zeta potential measurement. Our methodology based on first-principles calculations enables determining surface charge states quantitatively in the atomic and electronic level.

Conflicts of interest

There are no conflicts of interest to declare.

Acknowledgements

References

1 T. Noshi, T. Yoshikawa, M. Ikeuchi, Y. Dohi, H. Ohgushi, K. Horiuchi, M. Sugimura, K. Ichijima and K. Yonemasu, *J. Biomed. Mater. Res.*, 2000, **52**, 621–630.
2 H. Ohgushi, M. Okumura, S. Tamai, E. C. Shors and A. I. Caplan, *J. Biomed. Mater. Res.*, 1990, **24**, 1563–1570.
3 Y. Kuboki, H. Takita, D. Kobayashi, E. Tsuruga, M. Inoue, M. Murata, N. Nagai, Y. Dohi and H. Ohgushi, *J. Biomed. Mater. Res.*, 1998, **39**, 190–199.
4 A. H. Choi and B. Ben-Nissan, *Nanomedicine*, 2007, **2**, 51–61.
5 T. Kawasaki, *J. Chromatogr. A*, 1991, **544**, 147–184.
6 G. Yin, Z. Liu, J. Zhan, F. Ding and N. Yuan, *Chem. Eng. J.*, 2002, **87**, 181–186.
7 H. M. Kim, T. Himeno, T. Kokubo and T. Nakamura, *Biomaterials*, 2005, **26**, 4366–4373.
8 H. M. Kim, T. Himeno, M. Kawashita, T. Kokubo and T. Nakamura, *J. R. Soc., Interface*, 2004, **1**, 17–22.
9 I. S. Harding, N. Rashid and K. A. Hing, *Biomaterials*, 2005, **26**, 6818–6826.
10 S. V. Dorozhkin, *J. Colloid Interface Sci.*, 1997, **191**, 489–497.
11 M. Aizawa, T. Matsuura and Z. Zhuang, *Biol. Pharm. Bull.*, 2013, **36**, 1654–1661.
12 F. Ryuichi and K. Yoshinori, *Biochim. Biophys. Acta, Gen. Subj.*, 1991, **1075**, 56–60.
13 K. Kandori, H. Hamazaki, M. Matsuzawa and S. Togashi, *Adv. Powder Technol.*, 2014, **25**, 354–359.
14 T. Kanno, T. Sendai, K. Tada, J. Horiuchi and T. Akazawa, *Phosphorus Res. Bull.*, 2007, **21**, 25–30.
15 G. Kawachi, T. Watanabe, S. I. Ogata, M. Kamitakahara and C. Ohtsuki, *J. Ceram. Soc. Jpn.*, 2009, **117**, 847–850.
16 Z. Zhuang, T. J. Fujimi, M. Nakamura, T. Konishi, H. Yoshimura and M. Aizawa, *Acta Biomater.*, 2013, **9**, 6732–6740.
17 Z. Zhuang, H. Yoshimura and M. Aizawa, *Mater. Sci. Eng., C*, 2013, **33**, 2534–2540.
18 G. Bernardi, M.-G. Giro and C. Gaillard, *Biochim. Biophys. Acta, Protein Struct.*, 1972, **278**, 409–420.
19 G. Bernardi and T. Kawasaki, *Biochim. Biophys. Acta, Protein Struct.*, 1968, **160**, 301–310.
20 T. Kawasaki, *J. Chromatogr. A*, 1974, **93**, 313–335.
21 T. Kawasaki, *J. Chromatogr. A*, 1978, **151**, 95–112.
22 W. E. Brown, *Nature*, 1962, **196**, 1048–1050.
23 M. Aizawa, A. E. Porter, S. M. Best and W. Bonfield, *Biomaterials*, 2005, **26**, 3427–3433.
24 M. Jevtić, M. Mitrić, S. Škapin, B. Jančar, N. Ignjatović and D. Uskoković, *Cryst. Growth Des.*, 2008, **8**, 2217–2222.
25 K. Sato, T. Kogure, H. Iwai and J. Tanaka, *J. Am. Ceram. Soc.*, 2004, **85**, 3054–3058.
26 C. A. Ospina, J. Terra, A. J. Ramirez, M. Farina, D. E. Ellis and A. M. Rossi, *Colloids Surf., B*, 2012, **89**, 15–22.
27 F. Chiatti, M. Corno, Y. Sakhno, G. Martra and P. Ugliengo, *J. Phys. Chem. C*, 2013, **117**, 25526–25534.
28 K. Sato, Y. Suetsugu, J. Tanaka, S. Ina and H. Monma, *J. Colloid Interface Sci.*, 2000, **224**, 23–27.
29 Y. Sakhno, P. Ivanchenko, M. Iafisco, A. Tampieri and G. Martra, *J. Phys. Chem. C*, 2015, **119**, 5928–5937.
30 F. Chiatti, M. Delle Piane, P. Ugliengo and M. Corno, *Theor. Chem. Acc.*, 2016, **135**, 1–15.
31 R. Astala and M. J. Stott, *Phys. Rev. B: Condens. Matter Mater. Phys.*, 2008, **78**, 075427.
32 G. Kresse and J. Furthmüller, *Comput. Mater. Sci.*, 1996, **6**, 15–50.
33 J. P. Perdew, K. Burke and M. Ernzerhof, *Phys. Rev. Lett.*, 1996, **77**, 3865–3868.
34 M. I. Kay, R. A. Young and A. S. Posner, *Nature*, 1964, **204**, 1050–1052.
35 K. Mathew, V. S. C. Kolluru, S. Mula, S. N. Steinmann and R. G. Hennig, *J. Chem. Phys.*, 2016, **151**, 234101.
36 K. Mathew, R. Sundararaman, K. Letchworth-Weaver, T. A. Arias and R. G. Hennig, *J. Chem. Phys.*, 2014, **140**, 084106.
37 D. Zahn and O. Hochrein, *Phys. Chem. Chem. Phys.*, 2003, **5**, 4004–4007.
38 C. Park, P. Fenter, Z. Zhang, L. Cheng and N. C. Sturchio, *Am. Mineral.*, 2004, **89**, 1647–1654.
39 A. Pareek, X. Torrelles, K. Angermund, J. Rius, U. Magdans and H. Gies, *Langmuir*, 2008, **24**, 2459–2464.
40 P. Giannozzi, S. Baroni, N. Bonini, M. Calandra, R. Car, C. Cavazzoni, D. Ceresoli, G. L. Chiarotti, M. Cococcioni, I. Dabo, A. D. Corso, S. de Gironcoli, S. Fabris, G. Fratesi, R. Gebauer, U. Gerstmann, C. Gougoussis, A. Kokalj, M. Lazzeri, L. Martin-Samos, N. Marzari, F. Mauri, R. Mazzarello, S. Paolini, A. Pasquarello, L. Paulatto, C. Sbraccia, S. Scandolo, G. Sclauzero, A. P. Seitsonen,

A. Smogunov, P. Umari and R. M. Wentzcovitch, *J. Phys.: Condens. Matter*, 2009, **21**, 395502.

41 R. M. H. Verbeek, H. Steyaer, H. P. Thun and F. Verbeek, *J. Chem. Soc., Faraday Trans. 1*, 1980, **76**, 209–219.

42 T. Kubota, A. Nakamura, K. Toyoura and K. Matsunaga, *Acta Biomater.*, 2014, **10**, 3716–3722.

43 K. Matsunaga and A. Kuwabara, *Phys. Rev. B: Condens. Matter Mater. Phys.*, 2007, **75**, 014102.

44 K. Matsunaga, *Phys. Rev. B: Condens. Matter Mater. Phys.*, 2008, **77**, 104106.

45 E. McCafferty, *Electrochim. Acta*, 2010, **55**, 1630–1637.

46 D. J. Kim, H. Kim and J. K. Lee, *J. Mater. Sci.*, 1998, **33**, 2931–2935.

47 M. Robinson, J. A. Pask and D. W. Fuerstenau, *J. Am. Ceram. Soc.*, 1964, **47**, 516–520.

48 A. L. Valdivieso, J. L. R. Bahena, S. Song and R. H. Urbina, *J. Colloid Interface Sci.*, 2006, **298**, 1–5.

49 M. E. Labib and R. Williams, *Colloid Polym. Sci.*, 1986, **264**, 533–541.

50 K. Bourikas, J. Vakros, C. Kordulis and A. Lycourghiotis, *J. Phys. Chem. B*, 2003, **107**, 9441–9451.

51 C. Bellmann, C. Klinger, A. Opfermann, F. Böhme and H. J. P. Adler, *Prog. Org. Coat.*, 2002, **44**, 93–98.

52 A. Kasha, H. Al-Hashim, W. Abdallah, R. Taherian and B. Sauerer, *Colloids Surf., A*, 2015, **482**, 290–299.

53 D. A. Mahrouqi, J. Vinogradov and M. D. Jackson, *Adv. Colloid Interface Sci.*, 2017, **240**, 60–76.

54 S. L. S. Stipp, *Geochim. Cosmochim. Acta*, 1999, **63**, 3121–3131.

55 P. Rulis, H. Yao, L. Ouyang and W. Y. Ching, *Phys. Rev. B: Condens. Matter Mater. Phys.*, 2007, **76**, 245410.

56 A. Slepko and A. A. Demkov, *J. Chem. Phys.*, 2013, **139**, 044714.

57 P. Pulay, *Chem. Phys. Lett.*, 1980, **73**, 393–398.

58 H. Zhang and B. W. Darvell, *Acta Biomater.*, 2011, **7**, 2960–2968.

59 C. Kothapalli, M. Wei, A. Vasiliev and M. T. Shaw, *Acta Mater.*, 2004, **52**, 5655–5663.

60 J. Liu, X. Ye, H. Wang, M. Zhu, B. Wang and H. Yan, *Ceram. Int.*, 2003, **29**, 629–633.

61 J. Wang and L. L. Shaw, *Adv. Mater.*, 2007, **19**, 2364–2369.

62 E. Landi, G. Celotti, G. Logroscino and A. Tampieri, *J. Eur. Ceram. Soc.*, 2003, **23**, 2931–2937.

63 L. C. Bell, A. M. Posner and J. P. Quirk, *Nature*, 1972, **239**, 515–517.

64 E. Skwarek and W. Janusz, *Mater. Sci.*, 2016, **22**, 174–178.

65 S. Jana, A. Patra, S. Śmiga, L. A. Constantin and P. Samal, *J. Chem. Phys.*, 2020, **153**, 214116.

66 S. Jana, K. Sharma and P. Samal, *J. Phys. Chem. A*, 2019, **123**, 6356–6369.

67 S. Jana, L. A. Constantin and P. Samal, *J. Chem. Theory Comput.*, 2020, **16**, 974–987.

68 M. W. Chase, *NIST-JANAF Thermochemical Tables*, American Institute of Standards and Technology, New York, 4th edn, 1998.

69 D. D. Wagman, W. H. Evans, V. B. Parker, R. H. Schumm, I. Halow, S. M. Bailey, K. L. Churney and R. L. Nuttall, *J. Phys. Chem. Ref. Data*, 1982, **11**(suppl. 2), 38–267.

70 The VASP Manual – Vaspwiki, accessed July 2021, https://www.vasp.at/wiki/index.php/IBRION#cite_note-pulay:cpl:80-1.